

Synthesis and prototyping of a backdrivable parallel robot for metal finishing tasks

Pierre-Luc Beaulieu, Thierry Laliberté, Simon Foucault, Clément Gosselin *

Département de génie mécanique, Université Laval, 1065 avenue de la Médecine, G1V 0A6, Québec, Qc, Canada

ARTICLE INFO

Keywords:

Robotic finishing
Backdrivable robot
Parallel robot
Sensorless robot machining
Compliance head

ABSTRACT

This article presents the synthesis, control and experimental validation of a backdrivable three-degree-of-freedom translational mini robot used to control the interaction between a robot and a machined part during finishing tasks, such as polishing, sanding and deburring without requiring the use of a force/torque sensor. The mini robot acts as an active contact flange, allowing an industrial robot (the macro robot) to adapt to a part using an impedance control algorithm. Firstly, different three-degree-of-freedom parallel robot architectures are compared and the most suitable architecture is selected. Geometrical properties are chosen for the robot and the physical capabilities of the architecture are predicted to ensure that the design criteria are satisfied. An impedance control algorithm is then developed for the mini robot. The macro-mini system is formed by installing the mini robot on a gantry robot. Sanding tests are carried out in order to validate the performance of the system and the mini robot is compared to other contact flanges already available on the market. Finally, a method allowing the determination of the magnitude of the friction forces in the mini robot is presented and a preliminary friction compensation algorithm is developed. As opposed to existing tools, the novel mini robot proposed in this work is based on a compact parallel architecture, which makes it possible to ensure the backdrivability of the system in three directions. An impedance control algorithm can therefore be implemented thereby providing stability even with stiff environments and eliminating the need for a force/torque sensor.

1. Introduction

In several industrial manufacturing areas such as the aerospace and terrestrial transportation industry, the tooling industry and the fabrication of complex assemblies, the finishing of metallic parts is still performed manually [1]. Such tasks are tedious and pose a risk to the health and safety of workers [2], which is a significant incentive for the development of robotic finishing systems.

Metal finishing tasks require the control of the contact forces between the tool and the parts. Most of the concepts proposed in the literature for such tasks consist in using a robot equipped with a force/torque sensor at its end-effector, on which the tool is mounted [3]. An admittance control algorithm is then used to control the force in the direction normal to the contact while controlling the motion in tangential directions. Although this type of approach is viable, it poses several challenges. First, it is well known that in the presence of a stiff environment (such as metal parts), the admittance control algorithm can become unstable, leading to chattering [4], which can affect the quality of the parts or even prevent the tasks from being completed. Also, in practical applications, it can be difficult to find appropriate

force/torque sensors, which can make the control more difficult to implement, especially for tasks along edges such as deburring [5]. Moreover, multi-axis force/torque sensors are rather expensive, which makes it desirable to exclude them.

An alternative approach consists in using a compliant tool head (compliance head) mounted on the flange of a robot [6]. In this approach, the compliant head allows the adaptation of the motion to the geometry of the part while controlling the interaction force. In some systems, pneumatic actuators are used for compliance [7,8]. The compliant head typically includes a load cell (or a pressure sensor) that measures either the axial (vertical) or radial (lateral) force. Such an approach can provide good results for simple geometries. However, for more complex parts, controlling only one component of force is insufficient, which limits the potential applications. Several compliance heads are currently available on the market, such as the ACF-K from FerRobotics [9] and the PCFC-12-A-S1 from ATI Industrial Automation [10] for polishing, and the RC-340 [11], also from ATI Industrial Automation, for deburring. However, these tools allow the compliance either vertically or laterally, but not both at the same time. For finishing

* Corresponding author.

E-mail addresses: pierre-luc.beaulieu.5@ulaval.ca (P.-L. Beaulieu), thierry@gmc.ulaval.ca (T. Laliberté), Simon.Foucault@gmc.ulaval.ca (S. Foucault), gosselin@gmc.ulaval.ca (C. Gosselin).

<https://doi.org/10.1016/j.rcim.2024.102934>

Received 16 September 2024; Received in revised form 3 December 2024; Accepted 10 December 2024

Available online 20 December 2024

0736-5845/© 2024 The Authors. Published by Elsevier Ltd. This is an open access article under the CC BY-NC license (<http://creativecommons.org/licenses/by-nc/4.0/>).

tasks on complex parts, both vertical and lateral compliance might be desired. Furthermore, using a one-directional tool head means that it may have to be changed between various operations, increasing the manufacturing time. The development of passive two-degree-of-freedom mechanisms for deburring was proposed in the literature [12]. However, a device that can produce motion with all three dofs is desirable in order to cover all possible geometries.

In this paper, a third approach is proposed. It consists in designing a three-degree-of-freedom backdrivable mini robot to be mounted at the end-effector of a standard industrial robot. Similar concepts have been proposed in the literature [13,14] but the approach proposed here includes a backdrivable mini robot. This approach yields a macro-mini arrangement that is akin to robotic systems developed for physical human–robot interaction [15,16]. A parallel architecture is used for the design of the mini robot so that the actuators are fixed at its base. Using this approach, larger actuators can be used (since they are not mounted in series) and the reduction ratios can be low, which makes the robot backdrivable and compact. Since the mini robot is backdrivable, it can be controlled using an impedance control algorithm [17], without requiring any force/torque sensor or load cell. This is in contrast with other mini robots or tool heads [13,14], which are not backdrivable and which require force/torque sensors and admittance control, thereby being more prone to instability. Backdrivability is ensured by the use of a direct-drive or quasi direct-drive transmission, similarly to the approach taken in [18–20]. Also, for finishing tasks, where only interaction forces must be controlled, the mini robot can be limited to translational motions while the orientation is controlled by the macro robot. Indeed, the mini robot should be able to react promptly to changes in forces in all possible directions (full translational capability) while the orientation is not time-critical and can be handled by the macro-robot.

The article is structured as follows. In Section 2, the selection of the architecture of the mini robot is presented together with some design considerations. A prototype of the mini robot is also presented. In Section 3, the control of the mini robot is addressed using an impedance control algorithm. The experimental set-up used for the tests is described in Section 4 together with the first experimental results. Friction compensation is discussed in Section 5. Modifications to the design of the prototype, their impact on its physical capabilities and a stiffness study are presented in Section 6. Finally, conclusions are presented in Section 7.

2. Architecture of the mini robot

2.1. Performance requirements

As mentioned in the introduction, the proposed concept relies on the backdrivability of the mini robot. Therefore, the selected architecture must have low-friction backdrivability to adapt to the contact surfaces. Also, since the mini robot is to be mounted on the end-effector of a macro robot, it needs to be relatively compact and light. A maximum mass of 10 kg, including that of the polishing or deburring tool, is targeted so that it can be compatible with most commonly used cobots. A compact router used for polishing typically weighs approximately 2 kg (deburring tools are not considered here since they normally weigh less than a compact router). This estimation was confirmed by weighing a Makita compact router. Therefore, the maximum mass for the robot is less than 8 kg. On the other hand, the workspace of the mini robot does not need to be large since it is the macro robot's role to provide a large workspace. It is estimated that a workspace consisting of a cube with 4 cm edges should suffice to adapt to the contact tasks. Lastly, the mini robot must be able to exert the necessary contact forces at its end-effector. The mini robot is designed to perform two finishing tasks, namely, polishing (or sanding) and deburring. The contact forces needed for these tasks depend on the amount of material to be removed; however, it is possible to estimate the magnitude of the forces required

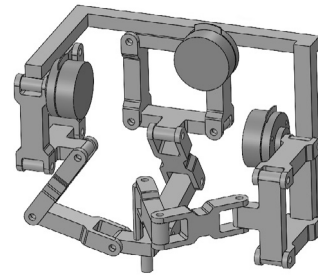


Fig. 1. CAD model of a tripteron with parallelograms.

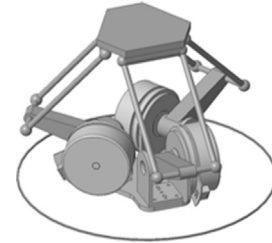


Fig. 2. CAD model of a Delta robot.

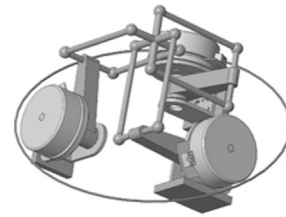


Fig. 3. CAD model of an Orthoglide.

for these finishing tasks. For polishing tasks, the forces needed can reach a magnitude of 50 N [13], in the direction of the Z axis. For deburring tasks, the forces vary between 5 N [21] and 20 N [12], in the direction of the X and Y axes. An average value of 10 N is chosen for the forces along the X and Y axes.

2.2. Selection of the kinematic architecture

Different three-degree-of-freedom translational parallel robot architectures are compared in order to select the most appropriate kinematic arrangement. Architectures in which the distal links of the legs are not subjected to bending or torsion are favoured, while those that include prismatic actuators are rejected as this type of actuator generally leads to more friction, compromising the backdrivability of the mechanism.

The first architecture considered is that of the tripteron [22], a translational robot with a 3- \underline{P} RRR architecture, where \underline{P} corresponds to an actuated prismatic joint and R to a passive revolute joint. One of the advantages of this architecture is that the three axes of the robot are decoupled, simplifying the control of the robot. Since the original architecture of the tripteron uses actuated prismatic joints, a variation of it that uses parallelograms and revolute actuators is rather considered [16]. This version of the tripteron has a 3- \underline{R} RRR architecture, where \underline{R} corresponds to an actuated parallelogram linkage. This version of the tripteron is illustrated in Fig. 1.

A second potential architecture is that of the Delta robot [23], shown in Fig. 2. It consists of a 3- \underline{R} \underline{R} \underline{R} architecture, where \underline{R} corresponds to an actuated revolute joint and \underline{R} corresponds to a passive parallelogram linkage. The Delta is a relatively compact translational

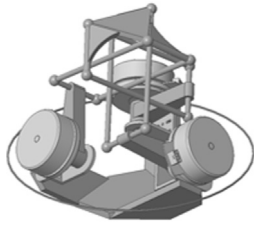


Fig. 4. CAD model of a modified version of the Orthoglide.

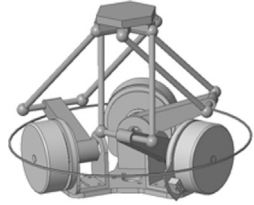


Fig. 5. CAD model of the tangential architecture.

architecture widely used in robotics. The next architecture considered is inspired by the Orthoglide [24], a 3-PR//R architecture robot, except that the prismatic actuators are replaced by revolute ones. The Orthoglide has the advantage of being isotropic in its neutral configuration and nearly isotropic around its neutral position. This architecture is illustrated in Fig. 3. Fig. 4 shows the next potential architecture, which consists of a modified version of the Orthoglide with revolute actuators. For this second version, the attachment points on the end-effector are modified, allowing to increase the length of the distal links of the robot legs, which has the effect of minimizing the variations of the mechanism's behaviour and maximizing its workspace. The last architecture considered is referred to as the tangential architecture. This architecture is inspired by a concept of a cable mechanism developed at Laval University [25]. It is also a 3-RR//R architecture. This architecture has the advantage that the robot's legs move minimally away from the centre of the mechanism during their movements, reducing the footprint of the robot. This architecture is illustrated in Fig. 5. Thus, five architectures of three-dof translational parallel robots are considered. They have been selected from the literature as the most promising ones for the proposed mini robot concept. They are qualitatively analysed in order to make a final selection. The tripteron is not chosen because of its rather small workspace to footprint ratio: the complexity of its base leads to a rather bulky robot. The same reasoning is applied to eliminate the first version of the Orthoglide. Indeed, one of the Orthoglide's disadvantages is that its legs can move far away from the centre of the mechanism during their movements, which increases the footprint of the robot. The second version of the Orthoglide is also eliminated. Maximizing the workspace is not a priority here since it is not an important design criterion for the intended task. Thus, there are two architectures left to consider: the Delta robot and the tangential architecture, which are quite similar. The tangential architecture is slightly more complex than the Delta and has the disadvantage of reducing the capacity to constrain moments since the distance between the pairs of distal links is not maximized. Therefore, the Delta architecture is selected.

2.3. Selection of the geometric parameters

Fig. 6 shows a schematic of a Delta robot. The Delta has four main components, each corresponding to a geometric parameter: the base with a radius R_b , the platform with a radius R_p , the proximal links of length L_1 and the distal links of length L_2 . The first step in designing the mini robot is to choose values for the aforementioned

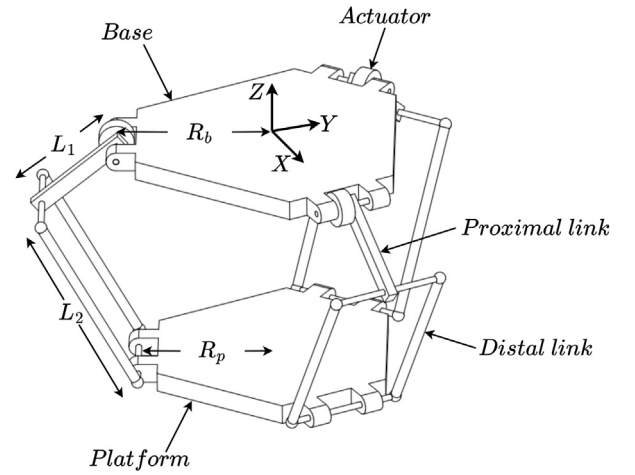


Fig. 6. Schematic of a Delta robot.

Table 1
Geometric parameters of the Delta.

Parameter	Length [cm]
R_b	8
R_p	7
L_1	5
L_2	10

geometric parameters, which allows to determine the joint torques that the actuators must provide in order to exert a certain force at the end-effector everywhere in the robot's workspace. It should be noted that the goal here is not to optimize the geometric parameters but rather to find a feasible combination of parameters that leads to a functional prototype satisfying the design criteria.

As a baseline, Maxon EC 90 flat motors are considered for the mini robot's actuators given their good mass to nominal torque ratio: the motors weigh 0.98 kg and provide a nominal torque of 0.963 Nm. Since the mass of the mini robot must remain under 8 kg including the mass of three actuators, it is critical to select motors with a good mass to nominal torque ratio. The EC 90 flat's ratio of about 1:1 should allow to satisfy both the maximum weight and minimum applicable contact forces criteria. Furthermore, these motors have previously been used for backdrivable parallel robots [20], making them prime candidates for the current application. In order to evaluate combinations of geometric parameters, actuated joint torques of approximately 1 Nm, which is close to the EC 90 flat's 0.963 Nm, are used. If necessary, a reduction stage can be added to the actuated joints in order to increase the forces that can be exerted at the robot's end-effector. Different combinations of feasible geometric parameters that lead to a compact architecture are tested. The final parameters chosen are presented in Table 1. These parameters are chosen for their promising results in terms of force transmission, footprint and workspace of the mini robot. As a reminder, the minimum workspace of the mini robot must correspond to a cube with 4 cm edges in order to allow compliance. Fig. 7 illustrates the workspace of the mini robot with the selected geometric parameters. The cube in the picture represents the minimum necessary workspace while the ring represents the base of the robot. Fig. 7 confirms that the minimum workspace criterion is met for the current geometric parameters: since the total workspace envelops the minimum workspace, the geometric parameters chosen allow to reach a sufficient workspace. In both figures, the 4 cm cube is centred under the base at heights ranging from 8 to 12 cm. This location is chosen for its convenience: with the current geometric parameters, when the proximal members of the mini robot are all parallel to its base, which is considered the neutral position

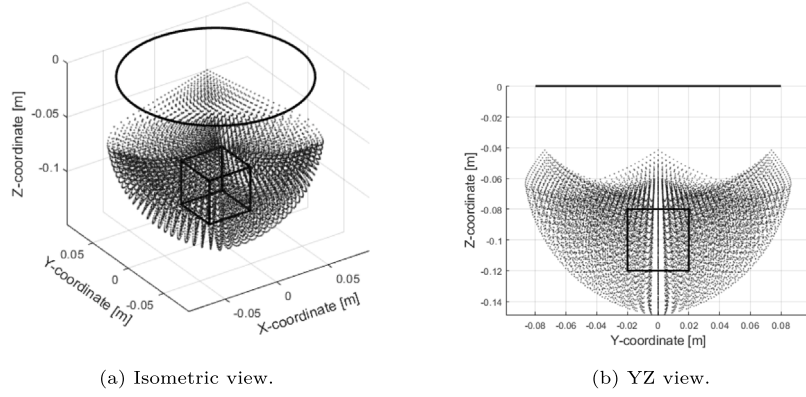


Fig. 7. Attainable workspace with the selected geometrical parameters.

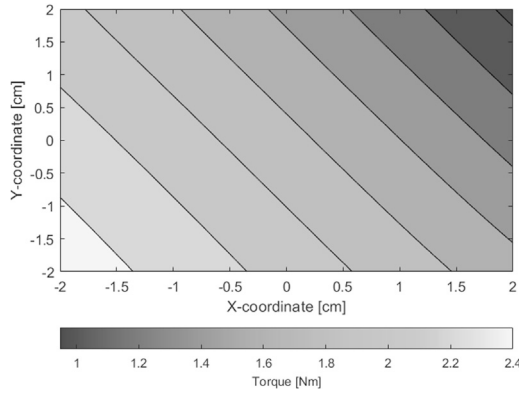


Fig. 8. Required torque at the centre of the workspace for one of the motors.

of the mini robot, the platform is located exactly 8 cm under the base. As per Section 2.1, the magnitude of the contact forces that the mini robot must be able to apply is 50 N vertically and 10 N laterally. In order to estimate the magnitude of the torques required at the actuators of the mini robot, an end-effector force $\mathbf{f} = [10, 10, -50]^T$ N is used; the torques required to exert this force everywhere in the workspace are then calculated. Fig. 8 shows the largest required torque at the actuators for different positions in the XY plane and a value of $Z = -10$ cm. It can be observed that the worst case scenario is reached at point $\mathbf{p} = [-2, -2, -10]^T$ cm and corresponds to a torque magnitude of 2.52 Nm. This indicates that if actuators with a nominal torque of 1 Nm are selected, then a reduction stage must be added at the actuated joints. A transmission system composed of pulleys and a toothed belt and with a reduction ratio of 3:1 is proposed, which preserves backdrivability. Indeed, a quasi-direct transmission mode is commonly used in robots with transmission ratios of up to 6:1 [20,26].

2.4. Prototype

Fig. 9 shows the first version of the prototype that was built as part of this project. The total mass of the prototype is 5.9 kg, which is far enough from the established maximum limit of 8 kg. This leaves flexibility to include a common polishing tool, such as a compact router, without exceeding the mass limit. The height of the prototype is 26.9 cm in its neutral configuration (when the proximal links are parallel to the base and the platform is located 8 cm below the base). The prototype also has a reasonable footprint. The aforementioned Maxon EC 90 flat motors are chosen for the mini robot's actuators. With a reduction ratio of 3:1, each motor provides 2.89 Nm, which is larger than the 2.52 Nm required. The total mass of the actuators is 2.94 kg,



Fig. 9. First version of the prototype of the mini robot.

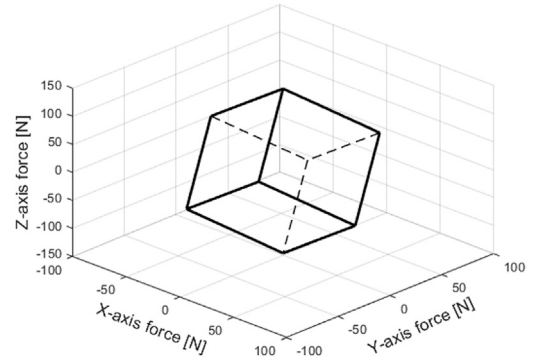


Fig. 10. Force space at the centre of the prescribed workspace.

which is about half of the total mass of the prototype, illustrating the necessity to choose motors with a good mass to nominal torque ratio such as the EC 90 flat.

The force capabilities of the mini robot are increased by the belt and pulley system (with a 3:1 reduction ratio). The force that the robot can apply is calculated at the centre of the prescribed workspace since this is the position around which the robot would normally operate. The force space, presented in Fig. 10, is obtained by calculating the forces exerted at this point in the workspace for different combinations of motor torques over the entire range of torques available for each motor (from -2.89 Nm to 2.89 Nm). The dotted lines in this figure represent the hidden edges of the parallelepiped. Fig. 10 shows that the maximum forces that the mini robot can theoretically exert at the centre of the prescribed workspace are 67.4 N along the X axis, 58.3 N along the Y axis, and 146.5 N along the Z axis. Thus, the robot can

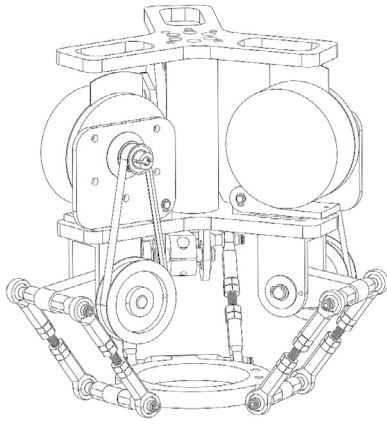


Fig. 11. Second version of the prototype of the mini robot.

amply exert the desired contact forces. In its current configuration, the maximum vertical force that the mini robot can exert is much greater than the lateral forces. If one wants to increase these lateral forces and does not need to exert such a large vertical force, it is possible to modify the geometric parameters (in particular the length of the proximal and distal members) in order to produce larger lateral forces by sacrificing some of the vertical force.

The mini robot's R/IJR joints were assembled using ball joint rod ends. Threaded rods were screwed in the rod ends' shank and shafts were inserted in the balls. In order to ensure that the mini robot is light enough to respect the maximum weight criterion, most of its parts are made of an aluminium alloy, except for the proximal links' shafts and distal links' threaded rods, which are made of a steel alloy to benefit from a higher yield strength. With a first batch of tests, it was determined that the backlash in the ball joint rod ends allowed the mini robot's platform to slightly rotate round the X and Y axes, which is undesirable. This caused the platform to vibrate when used with a compact router. A second version of the prototype was assembled where the R/IJR joints are spread further out, diminishing the backlash's impact and limiting the platform's rotation to an acceptable level. The distance between the middle axis of the two distal links of a R/IJR joint was increased from 39.64 mm to 78.53 mm. This second prototype, shown on Fig. 11, is used for the experiments of Section 4.

3. Control of the mini robot

The control algorithm includes three components, namely gravity compensation, impedance control and contact force control.

3.1. Gravity compensation

Fig. 12 shows a schematic of the forces involved in gravity compensation for one third of a Delta robot. The force \mathbf{f}_{g1} corresponds to the weight of the proximal link of one of the robot's legs, \mathbf{f}_{g2} corresponds to the weight of the distal link, and \mathbf{f}_{g3} corresponds to the combined weights of the platform and the payload attached to it. θ_i is the joint variable of one of the robot's legs, i.e., the angle of the proximal link. It should be pointed out that in the current application, the orientation of the base of the mini-robot can change since it is mounted at the end-effector of the macro robot. If the orientation of the base of the mini robot with respect to the fixed frame is given by matrix \mathbf{Q} , then the following scalar, noted β , provides the contribution of the motion of a point on the robot in the direction of gravity, namely

$$\beta = \mathbf{e}_k^T \mathbf{Q} \mathbf{e}_k \quad (1)$$

where \mathbf{e}_k is a unit vector in the direction of gravity in the fixed frame. The potential energy of the system is then given by

$$V = \beta \left(\sum_{j=1}^2 \sum_{i=1}^3 f_{gj} h_{ji} + f_{g3} h_p \right) \quad (2)$$

where h_{ji} corresponds to the elevation of the centre of mass of the j th link of the i th leg relative to the base in the robot's frame, while h_p corresponds to the elevation of the platform and payload in the same frame. The gravity compensation term is then obtained as

$$\boldsymbol{\tau}_g = -\frac{\partial V}{\partial \boldsymbol{\theta}} \quad (3)$$

For proximal links, the elevation h_{ji} is easily obtained. For the distal links, in order to simplify the derivation, half of the mass of the link is applied as a point mass at each of its end. The potential energy of the proximal link combined with one half of the mass of the distal link is then given by

$$V_{dpi} = -\left(f_{g1} + \frac{1}{2}f_{g2}\right) \beta r_{dp} \sin \theta_i \quad (4)$$

where

$$r_{dp} = \frac{m_p r_p + m_d L_1}{m_p + m_d} \quad (5)$$

where m_p and m_d respectively stand for the mass of a proximal and distal link, while r_p stands for the position of the centre of mass of a proximal link. The total potential energy for the three proximal links is therefore obtained as

$$V_{dp} = -\left(f_{g1} + \frac{1}{2}f_{g2}\right) \beta r_{dp} (\sin \theta_1 + \sin \theta_2 + \sin \theta_3). \quad (6)$$

Differentiating equation (6) with respect to each joint variable then yields

$$\boldsymbol{\tau}_{g,dp} = -\frac{\partial V_{dp}}{\partial \boldsymbol{\theta}} = \left(f_{g1} + \frac{1}{2}f_{g2}\right) \beta r_{dp} \begin{bmatrix} \cos \theta_1 \\ \cos \theta_2 \\ \cos \theta_3 \end{bmatrix} \quad (7)$$

The second half of the mass of the distal links is then combined with the platform and the payload. The Cartesian elevation of the centre of mass of the combined mass in the mini robot's frame is used and noted z . One has

$$V_c = -\left(f_{g3} + \frac{3}{2}f_{g2}\right) \beta z. \quad (8)$$

In Eq. (8), three halves of the mass of the distal links are added to the mass of the load. Differentiating equation (8) with respect to the Cartesian variable z yields

$$\mathbf{f}_c = -\frac{\partial V_c}{\partial \mathbf{x}} = \left(f_{g3} + \frac{3}{2}f_{g2}\right) \beta \mathbf{e}_z \quad (9)$$

where \mathbf{e}_z is a unit vector in the vertical direction in the mini robot's base frame. The torques that need to be applied by the motors in order to counteract this gravitational force is obtained using the robot's forward and inverse Jacobian matrices (respectively noted \mathbf{J} and \mathbf{K}). One has

$$\boldsymbol{\tau}_{g,c} = (\mathbf{J}^{-1} \mathbf{K})^T \mathbf{f}_c \quad (10)$$

The total gravity compensation torque is obtained with the sum of Eqs. (7) and (10). It should be pointed out that for the prototype presented in this work, the mass of the proximal and distal links is very small compared to the platform and tool. Therefore, the torques computed using Eq. (10) are largely dominant compared with those computed from Eq. (7). In fact, the latter might be neglected in practice.

3.2. Impedance control with a contact force

Since the mini robot must at the same time allow the adaptation of the macro robot to a part (compensation of geometric errors) and the application of machining forces, a control method slightly different from a typical impedance control algorithm must be developed. In fact, the machining forces must remain constant throughout a task to get an even surface finish, which is difficult to achieve using a typical

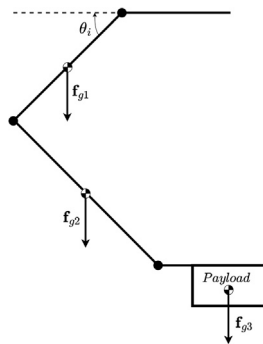


Fig. 12. Gravitational forces acting on the robot.

impedance control algorithm since the interaction force is dependent on the mini robot's Cartesian position [27]. It is pointed out again that no force/torque sensor is used in the control of the robot, which is possible because the robot is backdrivable. Figs. 13(a) and 13(b) illustrate the method envisioned for the robot. A virtual wall is programmed in the direction of the contact force \mathbf{f}_d . If, for some reason, such as when a contact force is applied, the mini robot's platform passes this wall, an impedance force \mathbf{f}_i is produced by the mini robot to bring its platform back to the other side of the wall. This impedance force is only present at and past the virtual wall and partially cancels the desired contact force \mathbf{f}_d , which is not a problem because the platform is not yet in contact with the machined part. When the mini robot comes in contact with the part, its platform moves to a section of its workspace not affected by the virtual wall; the force \mathbf{f}_i is not applied and only \mathbf{f}_d is exerted by the robot. It is possible to control the interaction that the mini robot has with the part by choosing the stiffness and damping of the robot around the virtual wall. Thus, the control algorithm provides three possible behaviours for the robot. First, in the directions where the mini robot must apply a desired contact force, a virtual wall is programmed (with a predetermined stiffness and damping), which allows the mini robot to adapt to the part while exerting the desired force. In the directions where the mini robot comes into contact with a surface without having to exert machining forces, the mini robot is programmed to have a low stiffness, allowing the mini robot to adapt to the part. Finally, in the directions where there is no contact between the mini robot and the part (which typically corresponds to the directions where the macro robot moves), the mini robot is programmed to be stiff in order to counteract the friction forces between the tool and the part. The control equation is therefore written as

$$\boldsymbol{\tau} = (\mathbf{J}^{-1}\mathbf{K})^T (\mathbf{S}(\mathbf{B}\Delta\dot{\mathbf{x}} + \mathbf{C}\Delta\mathbf{x}) + \mathbf{S}'(\mathbf{f}_d + \mathbf{S}_w(\mathbf{B}_w\Delta\dot{\mathbf{x}}_w + \mathbf{C}_w\Delta\mathbf{x}_w))) + \boldsymbol{\tau}_g) \quad (11)$$

where \mathbf{S} is a diagonal matrix whose diagonal entries are 1 in the directions where there is no contact force applied and 0 in the others, \mathbf{S}' is a diagonal matrix whose diagonal entries are 1 in the directions where there is a contact force applied and 0 in the others, \mathbf{S}_w is a diagonal matrix whose diagonal entries change from 0 to 1 when the virtual wall in a corresponding direction is crossed, \mathbf{B} is the prescribed damping matrix of the mini robot, \mathbf{C} is its stiffness matrix, $\Delta \mathbf{x} = (\mathbf{x}_d - \mathbf{x})$ is the difference between the platform desired and actual position, \mathbf{B}_w is the prescribed damping matrix for the virtual wall, \mathbf{C}_w is the stiffness matrix for the virtual wall, $\Delta \mathbf{x}_w = (\mathbf{x}_w - \mathbf{x})$, i.e., the difference between the position of the virtual wall \mathbf{x}_w and the actual position of the platform and $\boldsymbol{\tau}_g$ is the gravity compensation torque. The control scheme associated with Eq. (11) is shown in Fig. 14. In this scheme, $\mathbf{Z} = \mathbf{B}_s + \mathbf{C}$ is the impedance transfer function and $\mathbf{Z}_w = \mathbf{B}_w s + \mathbf{C}_w$ is the transfer function at the virtual wall.

3.3. Control of the macro-mini system

The task of the macro robot in the current macro-mini system is to position the mini robot close to the machined part so that the

mini robot can perform the finishing task while remaining within its workspace. Thus, a trajectory is given to the macro robot during which it allows the contact between the mini robot and the part. The mini robot then allows the macro robot to adapt to the part by moving in its workspace. The macro robot can then move in directions other than those where there is contact in order to perform its trajectory on the part. A more complicated algorithm could plan to move the macro robot according to the error on the position of the mini robot (in order to bring its platform to its desired position). Such an algorithm should provide a minimum position error threshold for the mini robot in order to avoid oscillations of the macro robot. Since the purpose of the tests performed in this project is to verify the proper functioning of the mini robot's adaptability and to verify that it applies the desired contact forces rather than to perfect the machining operations, a simple position control algorithm is programmed for the macro robot.

4. Experimental validation

In this work, the macro robot used is a Gantry robot. The experimental setup is shown in Fig. 15. The mini robot is attached at the Gantry's end-effector. Sanding tests, during which a compact router is added to the setup, are carried out in order to evaluate the system's performance.

Once the system's functionality is confirmed, the compact router is replaced by a force sensor at the end-effector of the mini robot to measure the contact forces applied by the prototype. It is recalled that the force sensor is not used by the controller. Its purpose is solely to provide some ground truth data in order to assess the capabilities of the system. Also, a 2 kg mass is added to simulate the mass of a typical compact router.

For the various tests, the workpiece consists of a wooden board attached to a table using clamps. A second board is fixed perpendicularly to the first in order to test the robot's lateral performance. In order to protect the integrity of the prototype, a safety system is added which stops the movement of the macro robot if the mini robot's end-effector deviates from its desired position beyond a given tolerated threshold.

4.1. Experimental validation of the capability of the robot to apply prescribed forces

Fig. 16 shows the results of a test in which the macro-mini system moves in a straight line along the workpiece while the mini robot is requested to apply a prescribed vertical force of 30 N. Several passes are made on the board one after the other; the macro-mini system accomplishes three round trips along the board. This figure shows an error of just over 5 N during the initial contact of the robot with the board, then an error of up to 4 N for the rest of the trajectory. Although the error is significant, it is deemed acceptable in a context of machining operations, where a very precise force control is not required. It is also recalled that the controller does not have access to the measured force. Fig. 17 shows the result of a second test in which the system moves in a straight line along the board, but this time while varying the prescribed vertical force between each pass. The error spike during the initial contact is still present. This figure shows that the robot exerts the required force relatively well even when it changes during the trajectory. It is also observed that the error on the force seems to increase when larger forces are prescribed. Fig. 18 shows the result of a test with multiple passes where the system moves along the second perpendicular board with a desired lateral force of 15 N. The observed error is around 2 N, which is deemed acceptable. Fig. 19 also shows the results of a test with multiple passes on the perpendicular board, but this time by varying the desired lateral force. The behaviour for a desired force of 10 N corresponds to what was observed during the preceding test. However, once the desired force is increased to 15 N, the error in the force applied is increased.

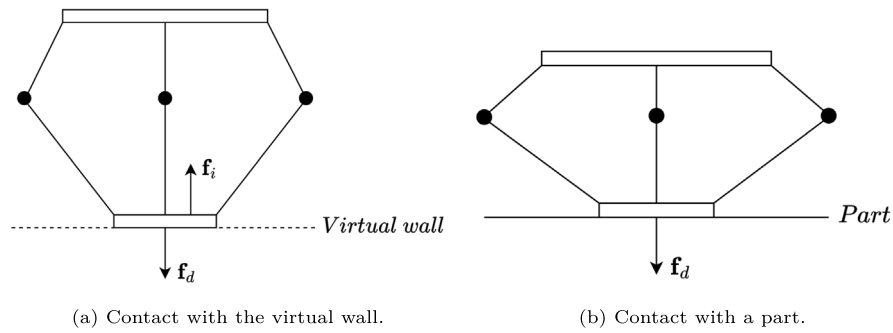


Fig. 13. Control of the mini robot while applying machining forces.

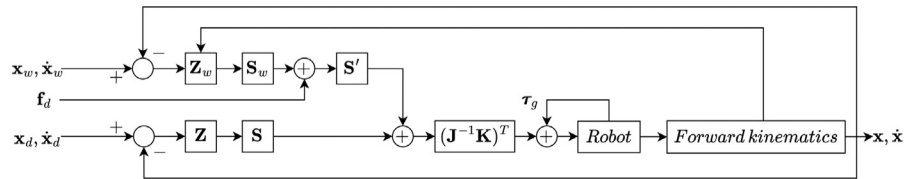


Fig. 14. Impedance control algorithm with contact forces and gravity compensation.

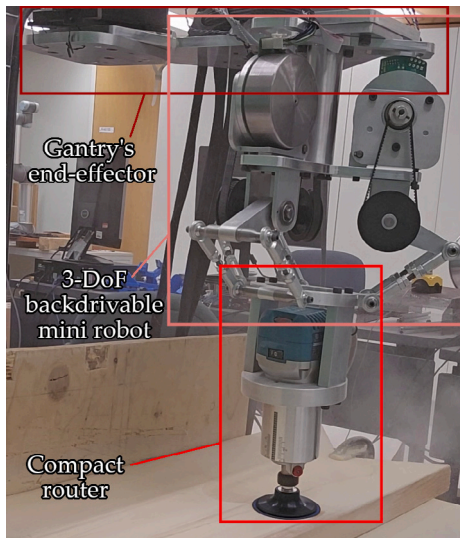


Fig. 15. Experimental setup.

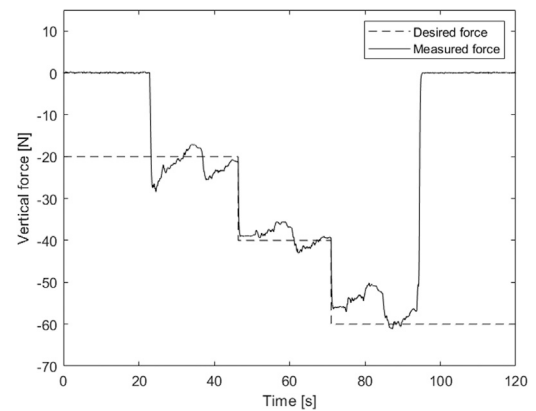


Fig. 17. Results for a test consisting of three round trips along the board without sanding with varying prescribed vertical forces between each pass.

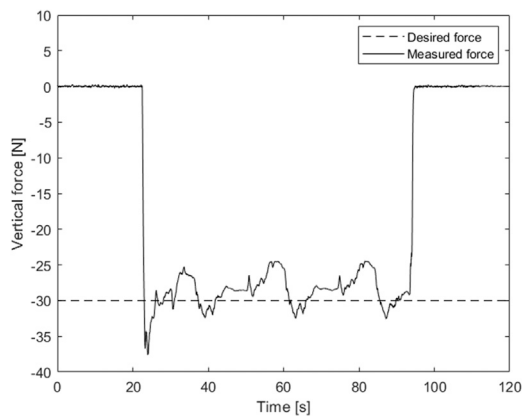


Fig. 16. Results for a test with a prescribed vertical force of 30 N for three round trips along the board without sanding.

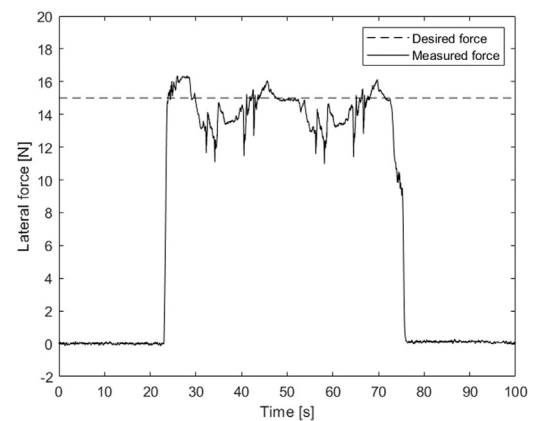


Fig. 18. Results of a test with a prescribed lateral force of 15 N for two round trips along the perpendicular board without deburring.

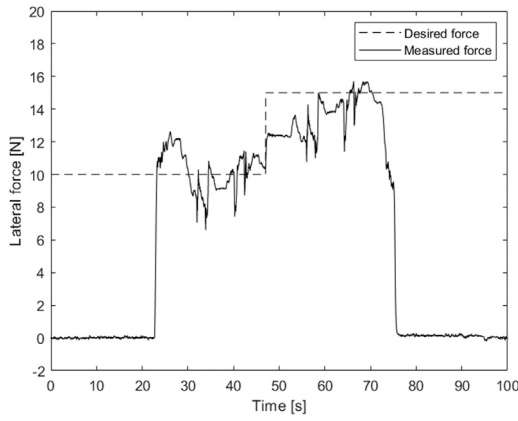


Fig. 19. Results of a test consisting of two round trips along the perpendicular board without deburring with varying lateral forces between each pass.

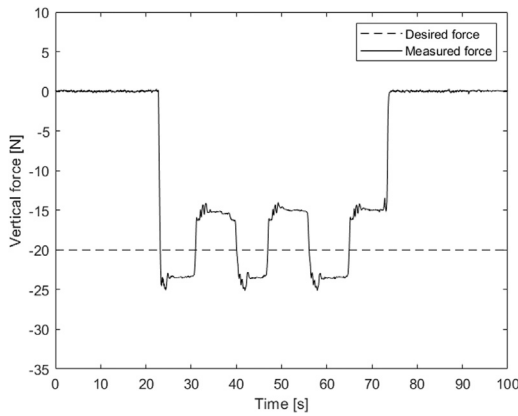


Fig. 20. Results of a vertical friction estimation test where the mini robot's vertical position is cyclically changed.

From the tests reported above, it can be observed that the mini robot is able to apply the desired contact forces with an acceptable precision. Part of the error observed may be caused by the system's inner friction, which is addressed in the next subsection. Indeed, since the controller is based on impedance control of a backdrivable system and since no force/torque sensor is used, friction in the system cannot be directly compensated by the controller. Friction compensation is addressed in an upcoming section of the paper. Moreover, since the error seems to increase for higher desired forces, further tests need to be carried out in order to evaluate the mini robot's performance for high contact forces. It should also be pointed out that, even though the applied force may vary within a certain range, the position of the robot is always precisely known from the joint encoders. Therefore, the robot can reach tightly prescribed positioning tolerances for finishing applications.

4.2. Inner friction

As mentioned above, it is observed that the system exhibits two behaviours when it comes to the error on the prescribed force, namely an initial spike during the contact with the part, which can be attributed to a lack of compensation for the system's dynamics in the control algorithm, and a lower more constant second error signal. These two behaviours are respectively referred to as friction in motion and friction at rest.

The current section presents the results of two tests carried out in order to calculate the system's vertical and lateral friction at rest. These tests consist in applying a contact force with the mini robot

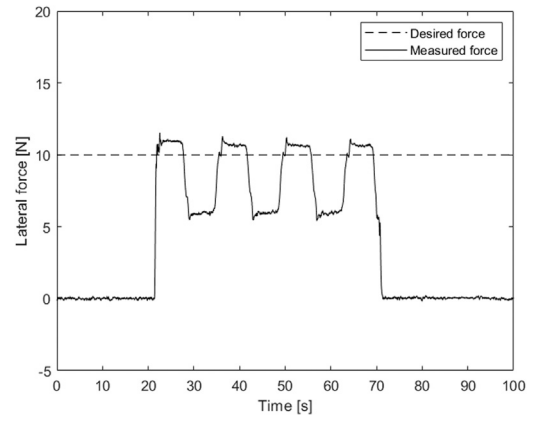


Fig. 21. Results of a lateral friction estimation test where the mini robot's lateral position is cyclically changed.

and cyclically varying the position of its end-effector in its workspace while still in contact with the workpiece by changing the macro robot's position. This allows us to measure the mini robot's inner resistance to motion. The result of such a test while applying a vertical force of 20 N is illustrated in Fig. 20. By halving the difference between the higher and lower forces measured at rest, the mini robot's vertical inner friction can be estimated: in this case, an average value of 3.75 N is measured. The same test is carried out in order to measure the lateral inner friction, this time by applying a 10 N force against the second perpendicular board. Fig. 21 shows the results of this test. The system's inner lateral friction's average value is 2.00 N. The measured force's asymmetry around the desired force here is caused by a calibration error, which will be discussed in more detail later in this article. The values calculated for the inner friction at rest are consistent with the measured errors in the tests reported in the preceding section, where vertical errors of 4 N and lateral ones of 2 N were observed. These results validate the assumption that part of the error is due to inner friction.

4.3. Maximum possible applied force

According to the design parameters selected and the static model, the theoretical maximum forces that the mini robot should be able to apply are 146.5 N vertically and 58.3 N laterally. Tests have been carried out to determine the practical maximum forces that the prototype can apply. For this set of experiments, the mini robot is requested to apply forces having a magnitude approaching that of the maximum theoretical forces. For these tests, the macro-mini robot makes several passes one after the other along the wooden board. Fig. 22 shows three graphs presenting test results for prescribed vertical forces of 80 N, 100 N and 120 N respectively. These three graphs clearly illustrate the observation made previously that the force error increases proportionally with the desired force, especially when the macro robot moves. For Fig. 22(a), the error is approximately 8 N. An error of 10% is acceptable for machining tasks, which shows that the mini robot can apply relatively high forces with a certain precision. Furthermore, Fig. 22(c) shows that the mini robot succeeds in applying vertical forces of 100 N. Thus, the errors in Figs. 22(a) and 22(b) do not come from the ability of the motors to provide the necessary forces; other sources of error are therefore present in the system.

One of the sources of error identified for high force tests is the friction caused by the contact between the tool and the part (in this case the wooden board). Indeed, by requesting the robot to apply large forces perpendicular to the board, the friction forces which oppose the movement of the macro-mini system along the board also increase. In order to counter these forces, high stiffness must be requested from the

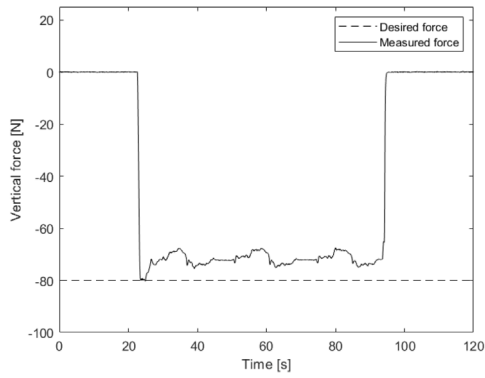
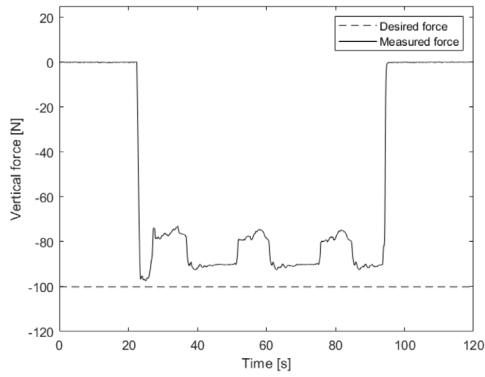
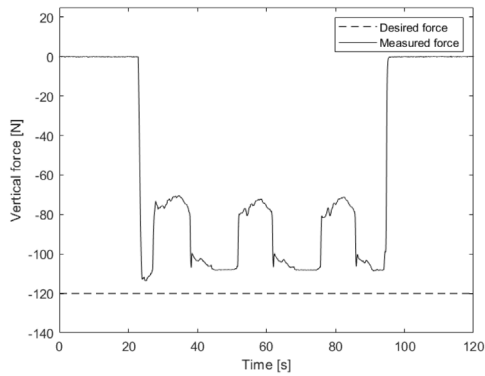
(a) $F = 80$ N.(b) $F = 100$ N.(c) $F = 120$ N.

Fig. 22. Measurement of the maximum applicable vertical force while in motion along the board without sanding for three prescribed contact forces.

robot in the directions of movement of the macro robot. A portion of the actuated joint torques that the robot should normally use to produce a normal force is therefore transferred to forces in another direction, reducing the machining force exerted, which explains the increase in the error proportionally with the increase of the desired force. Indeed, a larger normal force leads to a larger friction force between the end-effector and the board. This problem becomes even more significant when the desired force is raised to 140 N. In this case, the friction forces between the end-effector and the board are so large that, even with a high stiffness, the mini robot does not succeed in maintaining the platform close enough to the desired position. The platform goes beyond the limits imposed by the safety system, which causes the test to stop. The maximum force that the mini robot can exert therefore depends on the task. For a task in which it must apply a vertical force and move along a part, such as polishing, the mini robot can relatively

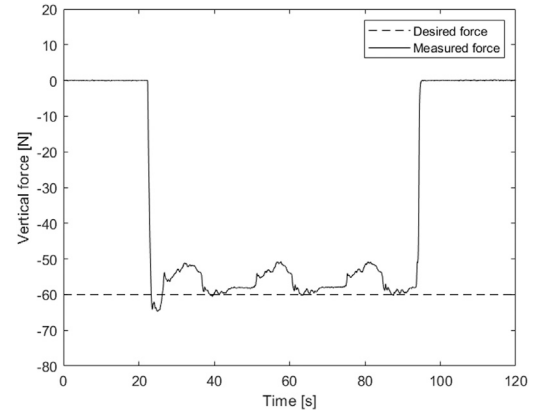


Fig. 23. Results for a test with a prescribed vertical force of 60 N for three round trips along the board without sanding.

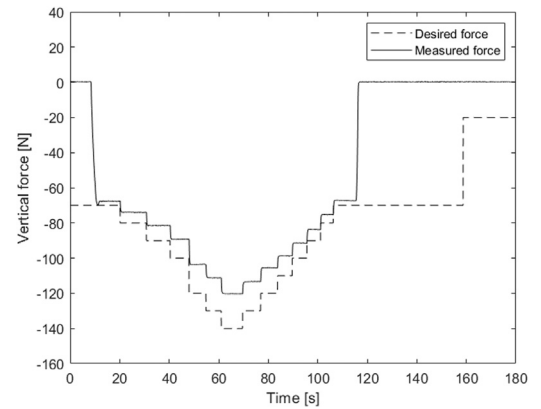


Fig. 24. Measurement of the maximum applicable vertical force at rest and without sanding.

reliably exert a force of up to 60 N, as shown in Fig. 23. Since the maximum force required to polish a piece of metal is estimated to be 50 N, the prototype is capable of performing its function and it can therefore be used as a compliance head. Since a significant part of the error in the measured forces comes from friction forces between the tool and the part, it becomes interesting to test the maximum force capacities of the mini robot when it simply rests on a surface. The results from such tests are shown in Fig. 24, which illustrates the portion of the error measured that does not come from the friction forces opposing the movement of the mini robot along the part. Once again, this error increases proportionally to the force requested. This graph still shows that it is possible to exert a contact force of 70 N with good precision. The error is attributed to two phenomena, namely the inaccuracies in the system's gravity compensation algorithm and a lack of calibration of the motors and drives used during the tests. Indeed, the force error seems to increase linearly with the desired force when it is above 50 N, which points to an error between the desired motor torques and those obtained. A motor calibration error could explain why the torques exerted by the motors are not as high as those prescribed, leading to lower Cartesian forces at the end-effector. As for the maximum lateral forces that the robot can exert, the same behaviour as for the vertical case is observed. Fig. 25 shows that forces of up to 40 N can be exerted, although not reliably. As shown in Fig. 18, the mini robot is however capable of exerting lateral forces of up to 15 N quite reliably. Since this value is within the range of the target force for a deburring task, the mini robot is able to perform its function, although this was not tested with the prototype.

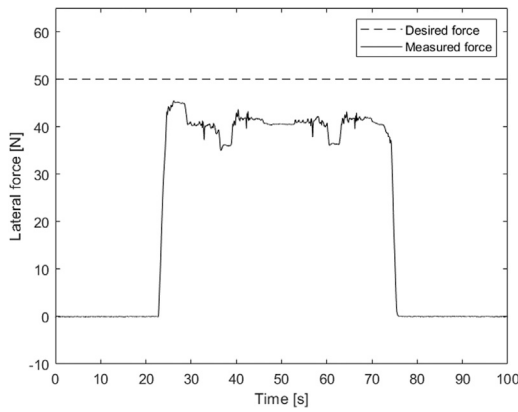


Fig. 25. Results for a test with a prescribed lateral force of 50 N for two round trips along the perpendicular board without deburring.

4.4. Comparison with other compliance heads

The mini robot is compared to commercially available compliant heads. The first is the ACF-K from FerRobotics, a vertical compliance head [9] that can apply a maximum tension or compression force of 100 N and which has a mass of 3.9 kg without tools attached. Another vertical compliant tool is the PCFC-12-A-S1 [10], which weighs 3.54 kg (without its motor) and can apply compliance forces between 8.9 and 85 N. The final compliance head compared is the RC-340, a lateral compliance head [11] that can apply a contact force of up to 42 N and which has a mass of 1.13 kg without tools attached. For these three products, compliance is implemented pneumatically. In comparison, the mini robot presented in this paper is theoretically capable of applying vertical forces of 146.5 N and lateral forces of 58.3 N. However, the tests carried out with the prototype showed that it can reliably exert forces of the order of 60 N vertically and 15 N laterally, which is lower than the forces provided by the commercial compliance heads. The mini robot has a mass of 5.9 kg without a tool, allowing compliance in three directions for an additional mass of only 2 kg compared to the ACF-K. Additionally, the entire mini robot system operates electrically rather than via pneumatics, which is an advantage since it makes the robot self sufficient (no external pneumatic source is needed). Moreover, the compliance of the mini robot can be programmed and varied in real-time, in all directions independently. Therefore it constitutes a much more versatile tool than the existing compliance heads. The extra mass of the mini robot is due to its compliance capabilities in all directions and to its backdrivability (which requires larger actuators). Nevertheless, it is believed that this extra mass is greatly justified by the advantages provided by the mini robot. It is also expected that improvements to the prototype could further increase its force capabilities.

5. Friction compensation

The experiments reported in Section 4 show that the mini robot exhibits two behaviours in terms of inner friction, namely the friction in motion and the friction at rest. In order to improve the performance of the robot, a friction compensation algorithm can be developed. The algorithm consists in estimating the friction based on two recorded data sets, namely one lateral and one vertical. The first step when estimating the friction forces in motion and at rest consists in determining whether the mini robot's end-effector is in motion or not when the measurement is taken. The velocity of the mini robot is estimated based on the motor encoders, using a moving average and a deadband to filter the noise. A value of either 1 or -1 is assigned for the direction of the end-effector's velocity at each instant of the data set, while a value of 0 is assigned if

the end-effector is at rest. With these values assigned, each measured force can be classified as a force in motion or at rest, providing us with data in order to estimate the friction in motion and at rest.

For the friction at rest, the calculation is simple. If the measured force is larger than the prescribed force, it is classified as maximum force data. Similarly, if the measured force is smaller than the prescribed force, it is classified as minimum force data. An average of the maximum and minimum forces is then calculated, yielding a mean maximum and minimum friction at rest. The friction at rest is calculated by halving the difference between the mean maximum and minimum friction at rest, similarly to what was done previously for the inner friction.

The calculation of the friction in motion is not as straightforward. The force in motion data vary much more than the data at rest. The choice is therefore made to only keep the local maxima for the calculation of the mean maximum friction in motion and only the local minima for the calculation of the mean minimum friction in motion. In practice, this choice leads to rather good average friction values. Other calculation methods might be appropriate, such as simply keeping the absolute maximum and minimum, but this leads to overestimating the system's friction. Finally, the friction in motion is calculated by halving the difference between the mean maximum and minimum frictions.

Once the friction in motion and at rest estimated for both the lateral and vertical directions are available, a model of the friction behaviour of the mini robot is established and can be applied to other datasets in order to predict the friction forces during a task. As with the previous analyses, the model prediction algorithm begins by calculating the velocity of the end-effector and assigning a value of 0, 1 or -1 to it. When the value assigned at a point in time is 1 or -1, the model adds or removes the friction in motion from the desired force according to the direction of the velocity in order to predict the behaviour in motion. When a value of 0 is assigned, then the friction at rest is added or removed. The choice to add or remove the friction force depends on the direction of the previous velocity perceived. In other words, the friction at rest is considered to be in the same direction as the last movement registered. This approach amounts to saying that the direction of the friction at rest does not change without there being friction in motion first. Thus, if the algorithm does not perceive a velocity in a direction opposite the current one, the friction at rest is always considered to be in the same direction. It therefore becomes important to choose the threshold values of the deadband carefully so as not to miss any change in the direction of the friction, while simultaneously ignoring small changes on the direction of the velocity, such as when the end-effector vibrates. This model is tested off-line on new datasets. Fig. 26 shows the contact force applied by the mini robot with the parasite friction predicted by the model and the real force measured for a vertical test with a desired vertical force of 30 N. Several passes are made along the wooden board. The model predicts the direction of the friction force throughout the test relatively well. However, in several instances, the model overestimates the magnitude of the force, which is expected when using a single dataset as a baseline to estimate the friction forces in the system. Since this test was performed off-line, the size of the moving average and the thresholds of deadband were adjusted in order to obtain good results. In a real-time context, such adjustments would not be possible which may deteriorate the results.

The model is also tested in a real-time experiment in order to better assess its effectiveness. Fig. 27 shows the results of a real-time prediction. As stated previously, in this case the parameters of the moving average and deadband cannot be chosen to obtain the best results possible, which explains the more significant fluctuation of the model. Nevertheless, the real-time model predicts the direction of friction well enough, showing that there is potential to further develop this algorithm. While the model developed is not perfect, it shows potential. The estimated lateral and vertical friction forces were calculated from one dataset each. By using more datasets, it would be possible to produce a more reliable and accurate model. This model

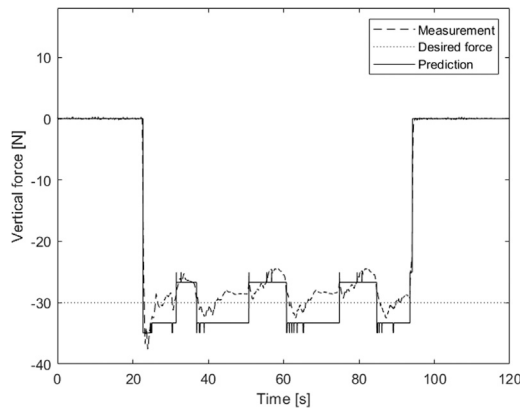


Fig. 26. Friction estimation using the model for an off-line vertical test consisting of several passes along the board without sanding.

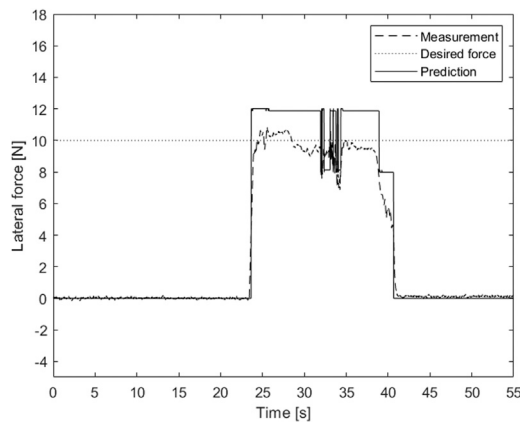


Fig. 27. Real-time prediction by the friction model for a lateral test consisting of a single pass along the perpendicular board without deburring.

could be complex enough to properly predict the behaviour of the mini robot at any time, no matter the situation in which it is used. It would thus be possible to avoid the problems of force overestimation. Such an algorithm would require analysing a large number of datasets, which would be more achievable using machine learning techniques. The optimization of the moving average and deadband parameters could also lead to better real-time results. Although, the friction compensation algorithm was not tested, it is believed that up to half of the friction could be compensated for, as per [20]. This hypothesis could be confirmed during further tests with the prototype.

6. Design modifications and stiffness study

As presented in Section 2.4, the lateral forces that the prototype can apply are much smaller than the vertical ones with the current geometric parameters. This leads to a lower maximum stiffness of the end-effector along the X and Y axes. Therefore, the mini robot sometimes lacks the necessary force to counter the friction between the tool and the machined part when the macro robot moves along these axes. It becomes interesting to modify the prototype's geometric parameters in order to transfer some of its vertical capabilities to the lateral directions, and to verify whether this makes it stiff enough for sanding and polishing tasks. In order to do so, the length of the proximal and distal links are changed as presented in Table 2. This third version of the prototype is shown in Fig. 28. With the new geometric parameters, the mini robot's end-effector is naturally closer to the base in its neutral position: the platform is located only 5.49 cm below the

Table 2

Parameter	Previous length [cm]	New length [cm]
R_b	8	8
R_p	7	7
L_1	5	7
L_2	10	9.7

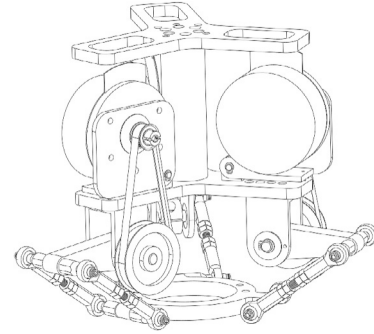


Fig. 28. Third version of the prototype of the mini robot.

base. This has the effect of increasing the applicable lateral forces while diminishing the vertical ones, which is the intended result.

Fig. 29 shows the workspace and force space with the modified geometric parameters. As it can be observed on Fig. 29(a), the minimum workspace consisting of a 4 cm cube has been moved up so it is located at elevations ranging from 5.49 to 9.49 cm below the mini robot's base. At the centre of this cube, the magnitude of the maximum forces that the prototype can theoretically exert are 85.4 N along the X axis, 73.9 N along the Y axis and 95.1 N along the Z axis, compared to 67.4 N along the X axis, 58.3 N along the Y axis and 146.5 N along the Z axis for the initial prototype. It is noted that the maximum vertical force has greatly decreased. However, since the prototype can still apply vertical forces larger than the target force of 50 N, this reduction is acceptable.

The inner friction of this third prototype was calculated with the method presented in Section 4.2. It is estimated that the average of the vertical friction is now approximately 3.02 N, and the average of the lateral friction is approximately 2.47 N. Several experiments were conducted in order to determine the prototype's maximum stiffness in each direction. These experiments consisted in prescribing increasing stiffness to the mini robot and then moving the end-effector manually while recording the displacement of the robot and the actuator torques. The rendered stiffness can be estimated by dividing the measured force in a direction by the end-effector's displacement (which is easily determined from the motors' encoders). For small displacements, the stiffness is not estimated since the division by small values leads to abnormally high values. Fig. 30 shows the estimated rendered stiffness for the Y axis of the prototype.

It can be observed that the values of the computed stiffness initially spike, then reach low values before spiking again. This behaviour can be explained by observing the position error (Fig. 31(a)) and prescribed motor torques (Fig. 31(b)) obtained during the experiment. When the end-effector's displacement becomes too high, the prescribed force increases and one of the motors quickly saturates, making it impossible to apply a large force, resulting in a low estimated stiffness. This can be confirmed by plotting the estimated rendered stiffness and the position error on the same graph, as presented in Fig. 32, which shows that the low estimated stiffness occurs when the end-effector's displacement reaches values higher than 15 mm. Moreover, this behaviour can be felt by hand : around its desired position, the end-effector can be very stiff, but then can quickly become easy to move past a certain displacement.

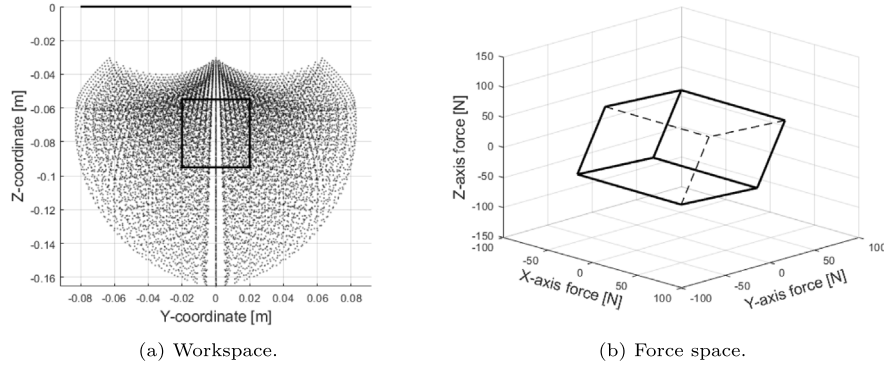


Fig. 29. Work and force spaces of the prototype with the modification to the geometric parameters.

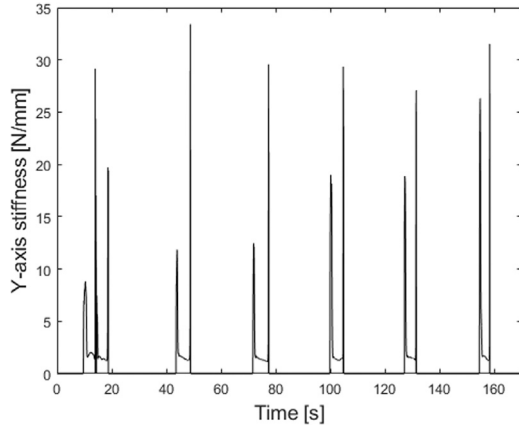


Fig. 30. Estimated rendered stiffness along the Y axis during a stiffness experiment with increasing prescribed stiffness.

In Fig. 31(b), the prescribed torques are never zero because of the gravity compensation. This figure also shows that when the prescribed stiffness is too high, the prescribed motor torques quickly alternate direction and increase even for small displacement, which makes the motors vibrate, leaving them in an unstable state.

Knowing the prototype's rendered stiffness behaviour, the maximum stiffness is taken during the initial spike since this represents the stiffness around the position at which the end-effector will operate. The second spike observed is not considered since the platform quickly goes back to its desired position when the force applied at the end-effector is removed, producing noisy and therefore unreliable data caused by the small measured displacement. The prototype's maximum stiffness is estimated to be approximately 26 N/mm along the X and Y

axes and 33 N/mm along the Z axis. These maximum stiffness values should be attainable as long as the mini robot's end-effector does not deviate too much from its prescribed position. This desirable outcome is achievable, as seen in Fig. 33, which presents the measured deviation of the end-effector along the X axis for two sanding tasks where the macro-mini system moves along a straight line in the direction of the mini robot's X axis while applying a contact force along the Z axis with the X axis stiffness set to its maximum. The compact router was slightly inclined so only a part of its sanding pad was in contact with the board, otherwise the pad would remove material on its full surface, which can create a discontinuity on the board and block the macro-mini system's movement. For both tasks, the end-effector's deviation from its intended position along the X axis was 0.2 mm. Furthermore, Fig. 34 presents the measured deviation of the end-effector along the Y axis for the same two sanding tasks. The Y axis stiffness was also set to its maximum. For the 20 N sanding task, the end-effector's deviation from its intended position along the Y axis was 0.5 mm, while the deviation was 1 mm for the 50 N task. The deviations are proportional to the reaction forces perceived, which are larger along the Y axis due to the higher velocity of the contact point of the pad in this direction : the X axis velocity corresponds to the gantry's velocity while the Y axis velocity corresponds to the peripheral velocity of the sanding pad. Nevertheless, in all four cases presented, the deviation is far from the 15 mm deviation that previously caused a decrease in stiffness. Therefore, the mini-robot should be stiff enough for sanding tasks at the target force.

7. Conclusion

This article presented the synthesis and control of a mini robot used as a compliance head for metal part finishing tasks. The objective was to design a prototype of a translational robot with three degrees of freedom following different design constraints, namely a limit on the

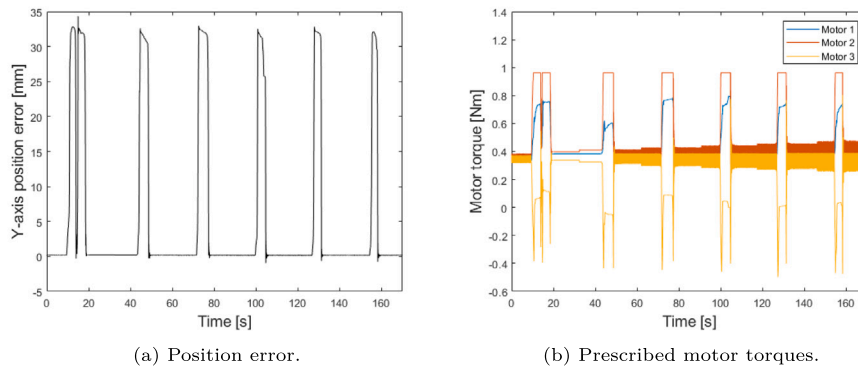


Fig. 31. Position error along the Y axis and prescribed motor torques during a stiffness experiment with increasing prescribed stiffness.

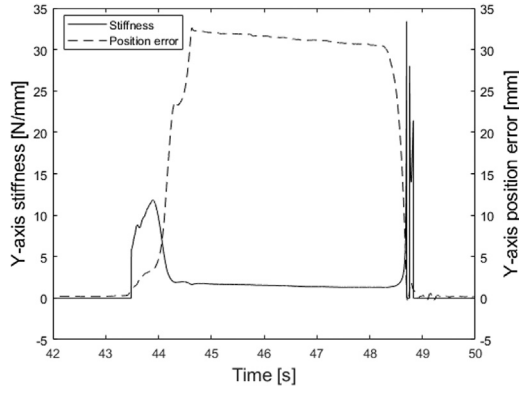


Fig. 32. Comparison of the estimated rendered stiffness and position error.

mass and volume of the robot, the possibility of applying the contact forces necessary to machine a part and a need to be backdrivable. The robot is to be mounted on the end-effector of a macro robot. The macro robot provides the large workspace while the mini robot is designed to adapt to the shape of the parts and provides the compliance required to perform the tasks.

Based on a selected parallel kinematic architecture and properly selected geometric parameters, a prototype was designed and built. The prototype is theoretically capable of exerting contact forces of approximately 60 N laterally and 145 N vertically at the centre of its workspace with a reduction ratio of 3:1. The design is compact and the prototype is backdrivable. A control algorithm is developed, making it possible for the mini robot to apply contact forces while adapting a macro robot to a part. The control algorithm is based on impedance control, which is made possible by the backdrivability of the robot. No force/torque sensor is needed with this approach.

The performance of the prototype was demonstrated through some tests carried out with a router mounted on the robot. The results of the tests showed that the mini robot can reliably apply contact forces of 15 N laterally and 60 N vertically, with respective force errors of 2.00 N and 3.75 N due to the robot's inner friction. While the mini robot's force capabilities are not as high as initially expected, they are sufficient for the machining tasks for which the prototype is designed.

A tentative friction compensation algorithm was presented. This algorithm can be used to build a reliable model of the friction forces present in the mechanism. Further developments of the algorithm could lead to a better model prediction in the future.

Finally, the prototype's geometric parameters are modified in order to increase the applicable lateral forces at the expense of the vertical ones. A stiffness study is conducted, which shows that a stiffness of 26 N/mm can be achieved laterally and 33 N/mm vertically. The mini robot is therefore stiff enough for sanding and polishing tasks.

The concept of mini robot presented in this paper constitutes a highly versatile tool for the finishing operations on metal parts. The robot's characteristics are fully programmable and can be used to provide the desired stiffness and damping in all motion directions, thereby leading to optimal metal finishing conditions.

Multimedia extension

A video demonstrating the experiments conducted with the prototype accompanies this paper. It presents two tests : one where the macro-mini system sands a wooden board along a straight line, demonstrating the vertical compliance made possible with the mini robot, and one where the system makes contact with a wall perpendicular to the aforementioned board, demonstrating both the vertical and lateral compliance capabilities.

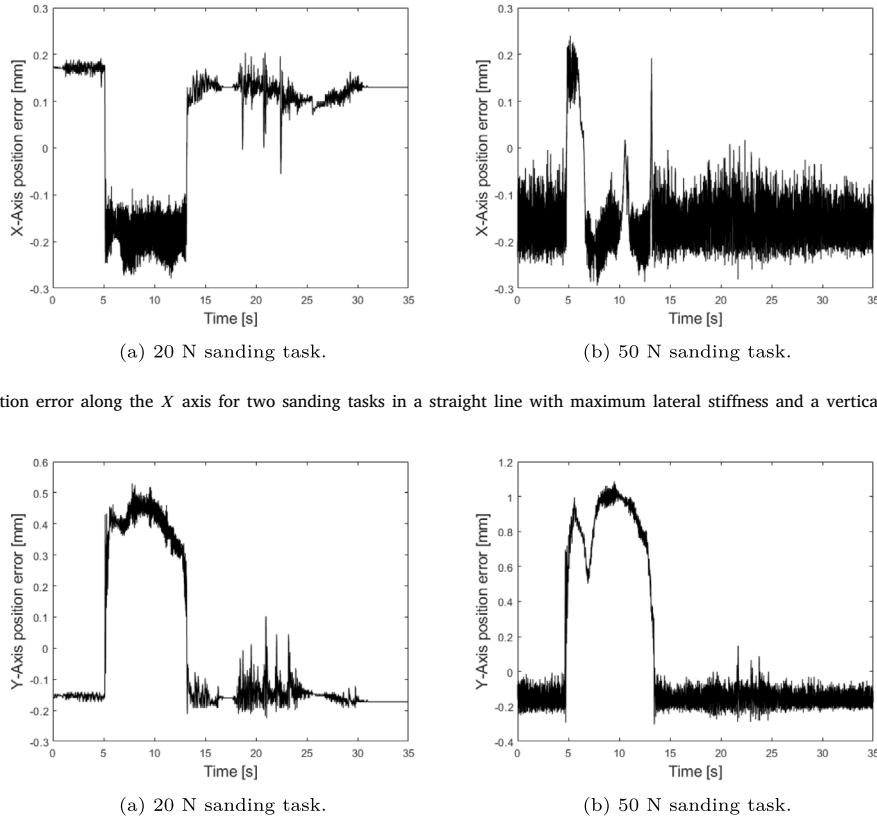


Fig. 33. Position error along the X axis for two sanding tasks in a straight line with maximum lateral stiffness and a vertical contact force.

Fig. 34. Position error along the Y axis for two sanding tasks in a straight line with maximum lateral stiffness and a vertical contact force.

CRediT authorship contribution statement

Pierre-Luc Beaulieu: Writing – original draft, Visualization, Validation, Software, Methodology, Investigation. **Thierry Laliberté:** Validation, Methodology, Investigation, Conceptualization. **Simon Foucault:** Validation, Software, Methodology, Investigation. **Clément Gosselin:** Writing – review & editing, Supervision, Methodology, Funding acquisition, Formal analysis, Conceptualization.

Declaration of competing interest

The authors declare that they have no known competing financial interests or personal relationships that could have appeared to influence the work reported in this paper.

Acknowledgements

The authors would like to acknowledge the financial support of National Research Council of Canada's METALTec industrial research group, the National Program Office, and the Metal Transformation Research and Innovation Consortium (CRITM).

Appendix A. Supplementary data

Supplementary material related to this article can be found online at <https://doi.org/10.1016/j.rcim.2024.102934>.

Data availability

No data was used for the research described in the article.

References

- [1] K. Saito, Finishing and polishing of free-form surface, *Bull. Japan Soc. Precis. Eng.* 18 (2) (1984) 104–109.
- [2] L. Punnett, D.H. Wegman, Work-related musculoskeletal disorders: the epidemiologic evidence and the debate, *J. Electromyography Kinesiol.* 14 (2004) 13–23.
- [3] J. Roy, L.L. Whitcomb, Adaptive force control of position/velocity controlled robots: Theory and experiment, *IEEE Trans. Robot. Autom.* 18 (2) (2002) 121–137.
- [4] M. Cordes, W. Hintze, Y. Altintas, Chatter stability in robotic milling, *Robot. Comput.-Integr. Manuf.* 55 (2019) 11–18.
- [5] I.F. Onstein, O. Semeniuta, M. Bjerkeng, Deburring using robot manipulators: A review, in: 2020 3rd International Symposium on Small-Scale Intelligent Manufacturing Systems, SIMS, 2020, pp. 1–7.
- [6] S. Gadringer, H. Gatringer, A. Mueller, Assessment of force control for surface finishing - an experimental comparison between universal robots UR10e and FerRobotics active contact flange, *Mech. Sci.* 13 (1) (2022) 361–370.
- [7] L. Liao, F. Xi, K. Liu, Modeling and control of automated polishing/deburring process using a dual-purpose compliance toolhead, *Int. J. Mach. Tools Manuf.* 48 (12) (2008) 1454–1463.
- [8] L. Liao, F. Xi, K. Liu, Adaptive control of pressure tracking for polishing process, *ASME J. Manuf. Sci. Eng.* 132 (1) (2010) 011015.
- [9] FerRobotics, ACF-K active contact flange kit, in: FerRobotics Compliant Robot Technology GmbH, Linz, Austria, 2022.
- [10] ATI Industrial Automation, Passive Compliant Force Control (PCFC) (Models 9150-PCFC-12), ATI Industrial Automation, Apex, USA, 2024.
- [11] ATI Industrial Automation, ATI Laterally-Compliant Robotic Deburring Tools Flexdeburr (Model 9150-RC-300 and -340 Series), ATI Industrial Automation, Apex, USA, 2023.
- [12] Y.-L. Kuo, S.-Y. Huang, C.-C. Lan, Sensorless force control of automated grinding/deburring using an adjustable force regulation mechanism, in: Proceedings of the 2019 International Conference on Robotics and Automation, ICRA, Canada, 2019, pp. 9489–9495.
- [13] A.E.K. Mohammad, J. Hong, D. Wang, Design of a force-controlled end-effector with low-inertia effect for robotic polishing using macro-mini robot approach, *Robot. Comput. Integr. Manuf.* 49 (2018) 54–65.
- [14] J. Chen, F. Jiang, Y. Xu, S. Li, Design and analysis of a compliant parallel polishing toolhead, in: Proceedings of the 2017 International Conference on Mechanical Design, ICDM2017, Czech Republic, 2018, pp. 1291–1307.
- [15] P.D. Labrecque, T. Laliberté, S. Foucault, M.E. Abdallah, C. Gosselin, uMan: A low-impedance manipulator for human–robot cooperation based on underactuated redundancy, *IEEE/ASME Trans. Mechatronics* 22 (3) (2017) 1401–1411.
- [16] N. Badeau, C. Gosselin, S. Foucault, T. Laliberté, M.E. Abdallah, Intuitive physical human–robot interaction: Using a passive parallel mechanism, *IEEE Robot. Autom. Mag.* 25 (2) (2018) 28–38.
- [17] L. Villani, J. De Schutter, Force control, in: B. Siciliano, O. Khatib (Eds.), *Springer Handbook of Robotics*, Springer, Berlin, Heidelberg, 2008, pp. 167–169.
- [18] K. Wen, T.S. Nguyen, D. Harton, T. Laliberté, C. Gosselin, A backdriveable kinematically redundant (6+3)-degree-of-freedom hybrid parallel robot for intuitive sensorless physical human robot interaction, *IEEE Trans. Robot.* 37 (4) (2020) 1222–1228.
- [19] D.V. Gealy, S. McKinley, B. Yi, P. Wu, P.R. Downey, G. Balke, A. Zhao, M. Guo, R. Thomasson, A. Sinclair, P. Cuellar, Z. McCarthy, P. Abbeel, Quasi-direct drive for low-cost compliant robotic manipulation, in: Proceedings of the 2019 International Conference on Robotics and Automation, ICRA, Canada, 2019, pp. 437–443.
- [20] T. Laliberté, M. Abdallah, C. Gosselin, A backdrivable 6-dof parallel robot for sensorless dynamically interactive tasks, *Robot. Comput. Integr. Manuf.* 86 (2024) 102642.
- [21] G.M. Bone, M.A. Elbestawi, R. Lingarkar, L. Liu, Force control for robotic deburring, *J. Dyn. Syst. Meas. Control* 113 (3) (1991) 395–400.
- [22] X. Kong, C.M. Gosselin, Kinematics and singularity analysis of a novel type pf 3-CRR 3-DOF translational parallel manipulator, *Int. J. Robot. Res.* 21 (9) (2002) 791–798.
- [23] R. Clavel, Device for the Movement and Positioning of an Element in Space (U.S. Patent No. 4 976, 582), U.S. Patent and Trademark Office, 1990.
- [24] D. Chablat, P. Wenger, Architecture optimization of a 3-dof translational parallel mechanism for machining applications, the orthoglide, *IEEE Trans. Robot. Autom.* 19 (3) (2003) 403–410.
- [25] D.S. Vu, E. Barnett, A.M. Zaccarin, C. Gosselin, On the design of a three-dof cable-suspended parallel robot based on a parallelogram arrangement of the cables, in: C. Gosselin, P. Cardou, T. Bruckmann, A. Pott (Eds.), in: *Cable-Driven Parallel Robots: Proceedings of the Third International Conference on Cable-Driven Parallel Robots, Mechanisms and Machine Science*, vol. 53, Springer, 2018, pp. 319–330.
- [26] P. Biswal, P.K. Mohanty, Development of quadruped walking robots: A review, *Ain Shams Eng. J.* 12 (2) (2021) 2017–2031.
- [27] T.M. Stepien, L.M. Sweet, M.C. Good, M. Tomizuka, Control of tool/workpiece contact force with application to robotic deburring, *IEEE J. Robot. Autom.* 3 (1) (1987) 7–18.